The Alaska Makushin Volcano 2016–2018 inflation and its potential relation to the 2020 earthquake swarm, from GNSS observations

Yitian Cheng [a,b,*], Ronni Grapenthin [a,b]

[a] Geophysical Institute, University of Alaska Fairbanks, 2156 Koyukuk Drive, Fairbanks, AK, United States
[b] Department of Geosciences, University of Alaska Fairbanks, 1930 Yukon Drive, Fairbanks, AK, United States

ARTICLE INFO

ABSTRACT

Makushin volcano on Unalaska Island along the Aleutian Chain in Alaska experienced a period of unrest from 2016 to 2020, including 2016–2018 surface inflation observed by 5 continuous Global Navigation Satellite System stations, and an earthquake swarm in the second half of 2020 consisting of hundreds of earthquakes, including two greater than M4. A Bayesian inversion of the geodetic data applied to a range of analytical source models suggests that the observed deformation pattern can be explained by an inflating pressure point source located 2 km east of the summit at a depth of approximately 5 km below sea level, with a chamber volume increase of approximately 0.004 km^3. A stress change analysis suggests that the 2016–2018 magma intrusion may have played a role in advancing the 2020 seismicity anomaly by modulating the regional stress field. Our study highlights the importance of stress transfer between magmatic and tectonic processes and the potential for using this information to better understand and mitigate the risk of volcanic eruptions.

1. Introduction

Volcanic unrest, the deviation of volcanic behavior from what is considered normal or baseline behavior, often lasting from several days to years, can ultimately transition into eruptions (Phillipson et al., 2013). The observation, identification, and interpretation of volcanic unrest can provide insight into volcanic processes, especially magmatic processes preceding an eruption, and thus provide opportunities for improving our ability to mitigate the hazards from volcano eruptions (Fernández et al., 2017). Common indicators to quantify a period of unrest include seismicity, gas emissions, thermal anomalies, crater morphological changes, and surface deformation (Pritchard et al., 2019). The last indicator is especially crucial in prolonged unrest as it can persist for years.

Surface deformation as precursory unrest stems from the fact that volcanoes can deform in response to subsurface magmatic mass movements or tectonic events (e.g., Segall, 2010; Biggs et al., 2014). Advances in geodetic data quality, the increasing availability of long-term continuous Global Navigation Satellite System (GNSS) observations (Herring et al., 2016; Blewitt et al., 2018; Grapenthin et al., 2022a) as well as the open availability of synthetic aperture radar (SAR) and the increasing ease of SAR interferometry, especially in the cloud (e.g.,

Lazecký et al., 2020; Grapenthin et al., 2022b), have made it possible to accurately observe and analyze phases of precursory surface deformation at many volcanoes (e.g., Ebmeier et al., 2018; Poland and de Zeeuw-van Dalfsen, 2021).

For example, Chaussard and Amelung (2012) analyzed Interferometric Aperture Radar (InSAR) observations from 2006 to 2009 and identified six volcanoes on the western Sunda Arc that were steadily inflating. These inflation patterns were all associated with shallow magma intrusions at depths ranging from 3 km to less than 1 km. Of the six inflating volcanoes, three erupted four months to two years after the observation period. A recent example of volcanic GNSS research is an in-depth integration and analysis of observations from the past two decades at Erebus volcano in Antarctica (Grapenthin et al., 2022a). This study elucidated the long-term subsidence pattern of the volcanic island, while also identifying distinct multi-year cycles characterized by inflation and deflation within the summit area of the volcano. Furthermore, it has been determined that the volcano was recently in an inflationary phase of this cycle and thus eruptive activity is likely to increase.

At Makushin Volcano (Aigagin in Aleut) in the central Alaska Aleutian Arc, Lu et al. (2002) reported uplift of 7 cm from 1993 to 1995 due to pre-eruptive inflation of a magma chamber by about 0.022 km^3, resulting in a small explosive eruption on January 30, 1995. Xue and

---

Freymueller (2020) resolve a period of deflation from 1996 to 2001 after this eruption, followed by inflation from 2001 to 2004. From 2004 to 2009 Lu and Dzurisin (2014) observed 10 mm/year of subsidence in InSAR data. Their modeling located both sources of deformation in the same location at ~6–7 km depth below the edifice, ~5 km east of the summit (Fig. 1). The last reported deformation at Makushin is an inflation period from 2016 to 2018, mentioned by Xue and Freymueller (2020).

This most recent episode of inflation did not yield an eruption. However, in 2020 a large earthquake swarm (Roman et al., 2020) struck an area just east of Makushin (Fig. 1). It started with an M4.2 earthquake on June 15th, followed by an M4.1 earthquake and several M3+ aftershocks. Thousands of small earthquakes were recorded in this swarm until September, all located ~12 km ESE of Makushin's summit, at 7–10 km depth below sea level. This swarm was the strongest since instrumental monitoring began in 1996. To explain the swarm, Lanza et al. (2022) resolve a local stress field change in seismic data, which they link to a potential dike intrusion. They suggested that magmatic processes are likely the primary driving mechanisms during the Makushin 2020 earthquake swarm.

Here we analyze and model the continuous GNSS records at Makushin volcano from 2014 to 2022 with a particular interest in the inflation from January 2016 to January 2018 and its potential relation to the 2020 seismicity. While Xue and Freymueller (2020) presented an analytical model for this time period, they only focused on tracking the magma volume history, assuming a previously resolved location at 7 km depth. We employ a Bayesian inversion approach (Grapenthin et al., 2022b; Angarita et al., in review) to resolve the posterior probability density functions of the parameter values for a range of potential source geometries. We then use the source to predict the stress change due to the intrusion, placing the deformation in the context of earthquake triggering. We suggest that intrusions into this magma reservoir encourage earthquakes in the region of the 2020 swarm. Understanding such time delay between unrest behaviors is helpful for comprehending volcano-tectonic events and developing effective hazard mitigation strategies.
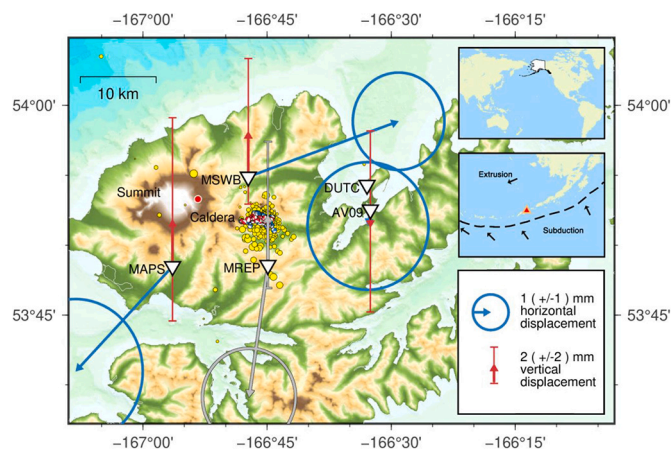

Fig. 1. Topographic relief map of Makushin volcano with the GNSS network and inferred offset vectors and their uncertainties (time interval: 2016/1/1–2018/1/1). All vectors are relative to the site DUTC, assumed stable. The red dot indicates the previous inflation sources (Lu et al., 2002; Lu and Dzurisin, 2014) and the yellow circles represent the June 2020 earthquake swarm. The beach balls are relocated events that are consistent (blue) and inconsistent (red) with the regional stress field, after Lanza et al. (2022). The data for MREP is tinted gray, indicating that it is not used in the inversion. The map inset top-right shows the location of Alaska (white). The middle-right panel shows the location of Makushin Volcano in the Aleutian Arc and the main tectonic processes of this area. (For interpretation of the references to colour in this figure legend, the reader is referred to the web version of this article.)

2. Background

Makushin Volcano, located on Unalaska Island on the eastern end of the the Aleutian volcanic arc in Alaska (Fig. 1), is a broad, truncated, ice-capped stratovolcano, about 1800 m high with a 16 km base diameter, as described by Miller et al. (1998). On the east slope of Makushin there is a breached summit caldera with a 3 km diameter. The tectonics are dominated by subduction of the Pacific Plate beneath the North American Plate at a convergence rate of 66 mm/year (DeMets et al., 1994), forming the Aleutian Megathrust. The coupling between subducting Pacific and overriding North American plates in the region is near zero (Elliott and Freymueller, 2020). Thus, we expect only insignificant interseismic strain build-up related deformation.

Makushin is one of the most active volcanoes in Alaska: through the 20th century, it experienced 7 confirmed and 4 unconfirmed explosion/eruption events (Dixon et al., 2020). The most recent eruption of Makushin occurred in January 1995, when a small explosive event produced a 2400-m-high ash cloud, steam, and a light brown ash plume (McGimsey and Neal, 1996). The Makushin edifice has mainly produced basalt and andesite lavas (Lerner et al., 2018), and the samples in recent major explosive eruptions are predominantly andesitic (Larsen et al., 2020).

Makushin Volcano experienced an unrest period of inflation between 2016 and 2018, followed by a strong seismic swarm in 2020. Due to the close spatial proximity (within 20 km) of the swarm and the center of inflation, we suspect that there may be a mutual coupling between the seismic activity and volcanic processes during this period.

Since Cayol et al. (2000) first introduced Coulomb stress modeling to volcano-earthquake interactions analysis (at Kilauea), several other studies have reported on suspected magma intrusion triggering earthquakes with similar methods. For instance, Baer et al. (2008) reported a two-month-long intense earthquake swarm in the East African Rift, concurrent with an eruption of the neighboring Ol Doinyo Lengai volcano. After analyzing InSAR deformation data and employing elastic Coulomb stress modeling techniques, they suggested that the earthquake swarm was largely induced by magma intrusion, which is also the reason for the eruption. Walter and Amelung (2006) used three-dimensional elastic Coulomb stress transfer to explain the volcano-earthquake interactions at Hawaii Mauna Loa volcano: magma intrusion can change the Coulomb stress along the fault plane, affecting seismic occurrence, while earthquakes can lead to clamping or unclamping of magma pathways, aggravating or relieving the constraints in the rift zone and influencing intrusions or even promoting eruptions.

The following two examples are more similar to the case of Makushin, as their earthquakes or swarms occurred with a time delay relative to surface deformation. The 1983 earthquake swarm on Long Valley, California, was likely caused by magma intrusion in 1982. Savage and Cockerham (1984) suggested that the intrusion resulted in a 3-bar tension on the slip plane, thus reducing frictional stress and promoting the earthquakes. Similarly, Thatcher and Savage (1982) analyzed the 1975–1981 inflation in Japan's Izu Peninsula, attributing it to magma intrusion. As a result of this intrusion, strike-slip shear stresses increased by about 1 bar, promoting failure and supporting the idea that the three earthquakes in the 1980s were encouraged by this intrusion process.

Apart from stress analysis, Pedersen et al. (2007) studied whether magma intrusion could trigger earthquake swarms by examining the ratio of accumulated seismic moment to released seismic moment. Elsworth and Voight (1995) used a quantitative static diffusion model to analyze in depth the possibility of large earthquakes being triggered by magma intrusion-induced changes in thermal pore fluid pressure. Here in this study, we investigate whether the earthquake swarm at Makushin in 2020 was triggered by the previous period of inflation by calculating and interpreting stress changes after inverting the deformation field for a magmatic source model.

3. Data and data analysis

As part of the network of ground based instrumentation for volcano monitoring and research in Alaska, the Alaska Volcano Observatory (AVO) established and operates a series of long-term continuous GNSS sites at Makushin volcano. The network (Fig. 1) consists of three sites 10–15 km from the summit that were installed in August 2011 (MSWB [Freymueller et al., 2011]) and July 2012 (MAPS, MREP; [Freymueller et al., 2012a,b]). Two sites, AV09 (installed in May 2004 as part of the Plate Boundary Observatory; UNAVCO Community, 2004) and DUTC (installed in August 2013; Freymueller and Grapenthin, 2013) are located near Dutch Harbor. The monuments for MAPS and AV09 are stainless steel short-braced monuments, whereas MREP and MSWB have concrete pillar monuments. All sites except DUTC, initially equipped with a Javad Sigma receiver, were initially operated with Trimble NetRS receivers and were upgraded to Septentrio PolaRx receivers in 2018 (MSWB, MAPS, MREP, DUTC), and 2019 (AV09). Except for AV09, which started out with a Trimble GPS-only choke ring antenna that was upgraded to multi-GNSS in 2019, all sites are equipped with Javad's choke ring antennas (RingAnt DM) with tall SCIGN radomes installed (SCIT). This means as of 2018/2019, the entire network is multi-GNSS capable. However, telemetry requirements result in prioritization of GPS signals.

We process GPS phase and range observations into daily position estimates (Fig. 2) following the same strategy as Grapenthin et al. (2022a). We use JPL's GipsyX software (Bertiger et al., 2020) with JPL's orbit and clock correction products, and International GNSS Service (IGS) antenna phase center corrections (Dow et al., 2009). When available, we use second order ionosphere corrections provided by JPL, with IGS products as a fallback. Troposphere delays are estimated and removed using the GPT2 model (Böhm et al., 2015). Ocean tidal loading corrections are based on the TPXO7.2 and ATLAS model (Egbert and Erofeeva, 2002), calculated with SPOTL (Agnew, 2012) in an Earth Center of Mass frame. We transform positions estimated from a non-fiducial reference frame to the 2014 version of the International Terrestrial Reference Frame (Altamimi et al., 2016). The residual antenna change offset at AV09 is inconsequential for the analysis of deformation between 2016 and 2018 and thus not estimated here (Fig. 2, green dashed line in AV09 panel).

Fig. 2 shows the east, north, and vertical components of the timeseries for the 4 Makushin GNSS sites relative to DUTC to eliminate background tectonic effects. We highlight in gray the dominant signal across all stations, which is the time period of inflation, starting at about 1 January 2016 and lasting until about 1 January 2018. Except for MREP, the timeseries for all stations outside of the inflation period do not reflect much additional deformation except for perhaps some mild seasonal effects (e.g., MSWB east). MREP, on the other hand, is very noisy. The deformation from 2016 to 2018 is detectable by eye in the north component, but its magnitude is difficult to determine given the large amplitude seasonal noise. The annual fluctuations at MREP are
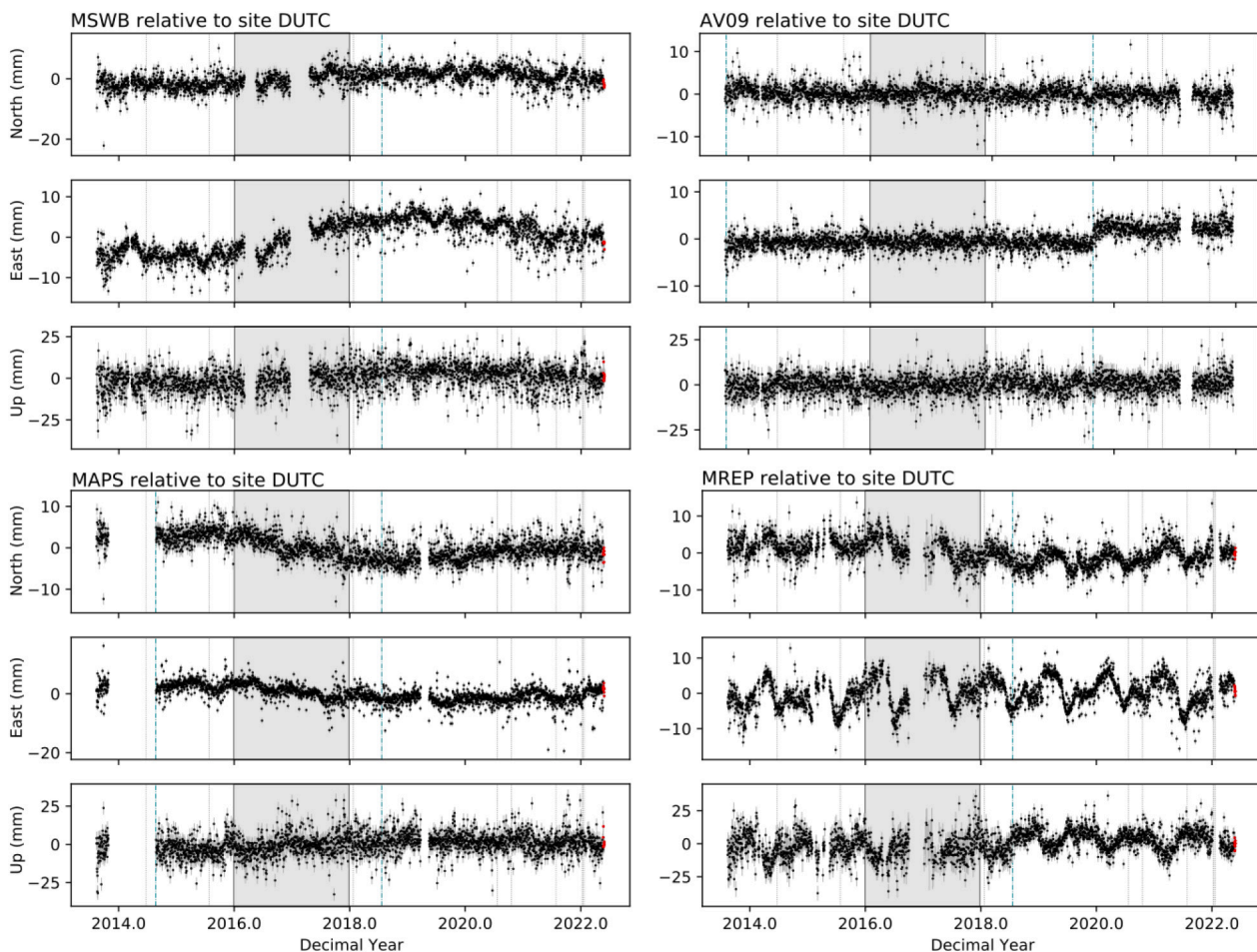

Fig. 2. Time series from late 2013 until mid-2022 of Makushin continuous GNSS stations MSWB, MAPS, and MREP relative to station DUTC in Dutch Harbor. AV09 near DUTC is included, showing that the sites behave similarly, except for the antenna change related offset. Gray area highlights the approximate time period of deformation (2016.00–2018.00). The vertical dotted lines indicate earthquakes in the vicinity, the vertical green dashed lines indicate times of antenna changes. Red dots in time series indicate solutions with rapid orbits. (For interpretation of the references to colour in this figure legend, the reader is referred to the web version of this article.)

most likely due to freeze-thawing effects from water in rock fractures that move the monument as rime icing is generally a shorter lived effect and snow loading is expected to be more regional. We attempted low-pass filtering to extract the 2016–2018 deformation at MREP, which did not yield satisfactory results given the low amplitude signal. Therefore, we ignored this station in the inversion.

To estimate the velocities for the time period between 1 January 2016 and 1 January 2018 we use the time series analysis software CATS, which consists of a linear procedure that can estimate combinations of intercept, slope, steps, and periodic terms and a nonlinear procedure that estimates the parameters for specific noise models (Williams, 2008). For each time series component of the chosen time interval we estimate a superposition of intercept, slope, and annual and semi-annual sine and cosine contributions, allowing us to retrieve a realistic velocity estimate over the 2 years. Estimation of a power-law noise model (Williams, 2008) results in conservative uncertainties for these time series model components. Fig. 1 shows the estimated velocities for all sites, capturing an outward trend away from the volcano in the horizontal components and upward motion in the vertical component relative to DUTC. We include the velocities for this time interval in Table 1. After the referencing, estimated horizontal velocities reach 5 mm/yr and the vertical velocities range between 2 and 3 mm/yr in the mountain range.

4. Modeling

4.1. Volcanic source inversion

Based on the deformation pattern (Fig. 1) and the activity history of the volcano (e.g., Lu and Dzurisin, 2014), we presume the observed deformation is caused by magma intrusion. Such observations are often examined with analytical source models (e.g., Segall, 2010; Sigmundsson et al., 2018) which provide (approximate) solutions for surface deformation due to subsurface magma dynamics. Analytical models are generally characterized by source shape and parameterized by geometry (location, strike, dip, finite dimensions) and a measure of strength (volume or pressure change).

One of the simplest magmatic source models is a pressurized point source embedded in a homogeneous elastic half-space, or a Mogi source, after Mogi (1958). It can be described with only 4 parameters: 3 for the location and one for the source strength, which is a combination of pressure change and source radius scaled by the rigidity of the hostrock and often expressed in terms of volume change (e.g., Sigmundsson et al., 2018). For instance, modeling subsurface volume increase or inflation with the Mogi model creates horizontal displacements away from the center of the source (projected on the surface), and vertical displacements that show uplift.

Other analytical models represent magmatic processes with different characteristics, predominantly captured in their primary geometry. The models we also tested include a McTigue source, representing a spherical magma chamber of finite size (McTigue, 1987), a Yang source, representing a finite ellipsoid-shaped chamber (Yang et al., 1988), and, as suggested by Lanza et al. (2022) as driving Makushin's 2020 seismicity: an Okada source, representing a dike or sill source (Okada, 1992). These models capture more complex geometries in chamber shapes and therefore require more parameters describing them. In addition to three parameters for position and one for source strength, the spherical model requires a fifth parameter for the radius of the magma reservoir. The ellipsoid and dike models also require parameters for size, aspect ratio, as well as their orientation in space (strike and dip). Thus, the McTigue model requires 5 parameters and the Yang/Okada models require 8 parameters each. The deformation fields generated by the different model geometries are distinct, especially for 3D deformation, so it is possible to infer magma system information from the observed deformation (see, e.g., Fig. 5 in Sigmundsson et al., 2018).

Here, we estimate the model parameters from the deformation observations to determine the character of the subsurface source. We can do this by solving a nonlinear inverse problem, as the forward models are nonlinear in at least some parameters. We frame this as a Bayesian problem where the probabilities of model parameters taking on certain values are characterized by the posterior distributions. As it can be challenging to obtain the complete posterior distribution for each parameter, we employ the Markov Chain Monte Carlo (MCMC) method to stochastically sample a reasonably large subset of the parameter space to approximate the posterior distribution. It has been shown that with a sufficiently large sample set, the posterior probability distribution of the samples can be close to the exact distribution of model parameters values (e.g., Aster et al., 2018 and references therein).

This methodology hinges on the stochastic ("Monte Carlo") construction of a Markov chain, a distribution that approximates the parameter's posterior. This sampling is generally implemented via an adaptive Metropolis-Hastings algorithm (e.g., Hastings, 1970; Aster et al., 2018; Haario et al., 2001). After obtaining a substantial number of samples, we discard highly correlated samples. We also remove a large number of initial values as these can be affected by the choice of the initial model parameters (burn-in). The remaining samples can be considered to represent a distribution consistent with the true model parameters. While MCMC does not require the model parameters to be independent, the convergence of the Markov Chain may be compromised when strong correlations exist among some parameters. (Aster et al., 2018).

We use the Python-based and fully object-oriented VMOD software (Angarita et al., in review.), which implements the MCMC through the PyMC library (Patil et al., 2010). VMOD is a Python-based versatile source model and inversion framework for geodesy, supporting all mainstream geodetic models and their combinations. In our MCMC inversion for Makushin, the burn-in period covers the first 100,000 samples and the subsampling stepsize is 1000. The number of total steps on the Markov chain is model-dependent: 1,100,000 for Mogi and McTigue models, 5,100,000 for Yang and Okada models as they are more complex.

4.2. Stress change modeling

After obtaining a model that represents the magma intrusion process at Makushin through the inversion described above, we estimated the stress changes induced by this intrusion using a finite element model (FEM).

We employed the COMSOL Multiphysics 6.0 software for the FEM simulation. We first constructed a model domain whose size significantly exceeds the scale of the Makushin magma system. This region was

Table 1

GNSS stations, their velocities (v), 2-year offset values (u) during periods of deformation, and offset uncertainties (σ). Corresponding with Fig. 1, velocities, offsets, and uncertainties are relative to DUTC. Here the positive values refer to east-, north-, or upward movement (directions indicated by indices).

site id	Lon (°)	Lat (°)	v_e (mm/yr)	v_n (mm/yr)	v_u (mm/yr)	u_e (mm)	u_n (mm)	u_u (mm)	σ_e (mm)	σ_n (mm)	σ_u (mm)
MAPS	−166.9405	53.8081	−2.66	−2.89	2.59	−5.32	−5.78	5.17	3.77	4.06	11.17
MREP	−166.7483	53.8096	−0.52	−3.63	2.76	−1.04	−7.26	5.52	2.61	2.75	8.04
MSWB	−166.7879	53.9147	4.13	1.53	2.50	8.26	3.06	5.01	2.57	2.73	8.01
AV09	−166.5418	53.8756	−0.07	−0.45	−0.99	−0.13	−0.89	−1.99	3.39	3.58	10.65
DUTC	−166.5485	53.9050	0	0	0	0	0	0	0	0	0

filled with a solid medium characterized by specific elastic parameters to represent the surrounding rock. We then introduced a cavity with designated shape and dimensions at positions resolved by the inversion within the surrounding rock to represent the magma source. The magma intrusion process was simulated by applying stress on the walls of this cavity. The model parameters (e.g., locations, dimensions, pressure) were set to the maximum a posteriori (MAP) values obtained from the inversion. The top surface of the model domain is explicitly defined as a free surface: this designation implies that the surface is not subjected to external stresses, allowing the material to deform freely without constraints. For the other surfaces, 'roller' constraints are employed, permitting displacement in the direction perpendicular to the boundaries while restricting movement within the plane of the boundaries. Our model is highly simplified, focusing exclusively on the stress in the surrounding rock from a static structural mechanics aspect only, excluding considerations like the rheological properties of magma, viscoelasticity of the surrounding medium, thermo-mechanical coupling (e.g., thermal expansion of the surrounding rock), and topographical influences. Moreover, since the surrounding rock is prestressed, the calculated stress tensors only represent stress change that is caused by magma intrusion and do not give total stress.

Upon acquiring the stress tensor field, further calculations can be conducted to better evaluate the effects of pressurization on crustal rocks, such as evaluation of the principal stress changes (e.g., Hooper et al., 2011) or the Coulomb stress changes (e.g., King et al., 1994). Assuming zero pore pressure change, the Coulomb stress change, $\Delta CFS = \Delta\tau + f\Delta\sigma$, is defined on faults of a given orientation, where $\Delta\tau$ is the change in shear stress, $\Delta\sigma$ is the change in normal stress, and f is the apparent coefficient of friction.

To evaluate the influence of Coulomb stress changes on earthquakes, it is essential to select the orientation of receiver faults that best represent the earthquake swarm. Following Lanza et al. (2022), we categorize earthquakes into two types: those consistent with the regional dominant stress environment (P-axis oriented NE-SW) and those that are inconsistent. Earthquakes consistent with the regional dominant stress environment are likely related to the subduction of the Pacific Plate under the North American Plate, and we adopt the strike of subduction as the orientation for receiver faults. For those that are inconsistent, we use the average strike of inconsistent strike-slip earthquakes from Lanza et al. (2022) as a representation (105°). Both types of receiver faults are modeled as left-lateral pure strike-slip faults.

Throughout our inversion and stress calculations, we treated the surrounding rock as a homogeneous elastic continuum, and a consistent set of elastic parameters was utilized: the Young's modulus was set to 10 GPa, and the Poisson's ratio was 0.25 (Heap et al., 2020). For the Coulomb stress change calculations, we set f to be 0.4. We adopted physical indication, where shear stress is positive in rake direction and normal stress is positive in tension.
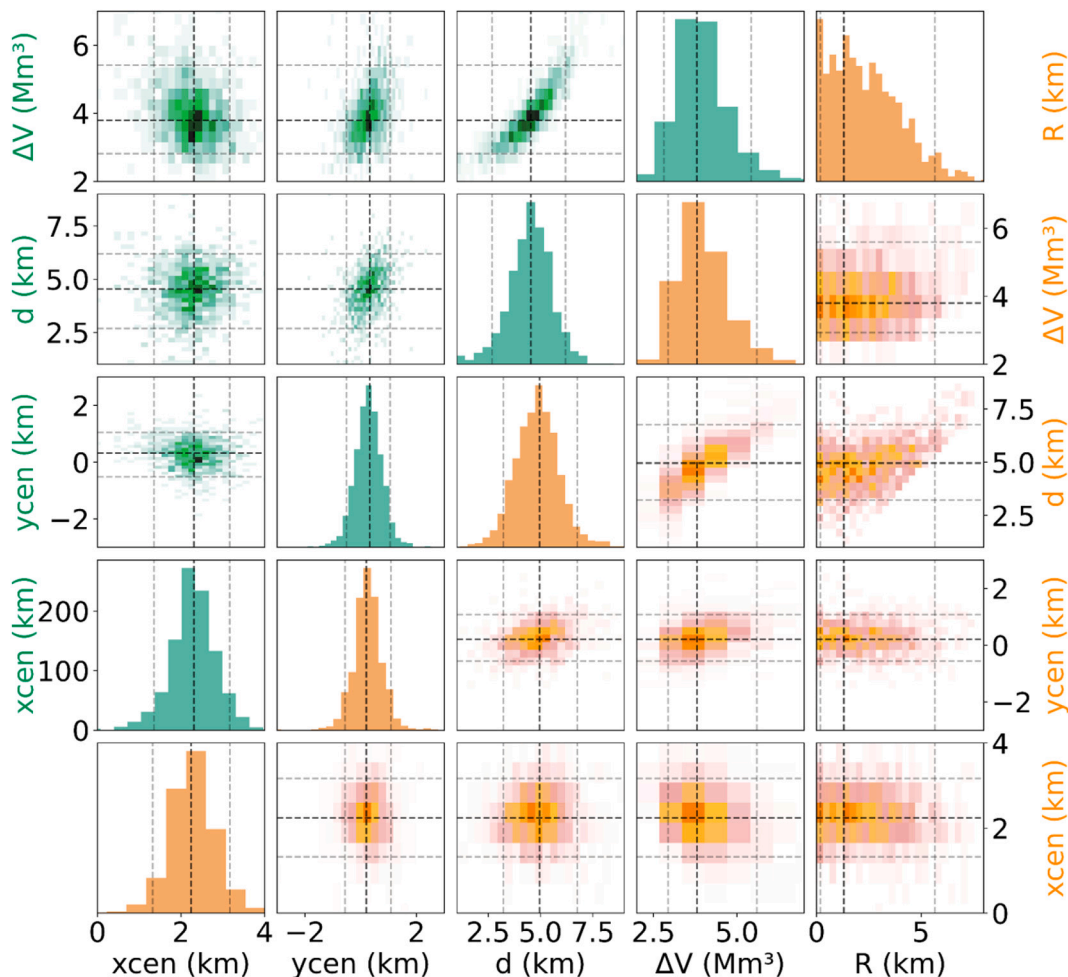

Fig. 3. Histograms of estimated probability density distribution of parameters for Mogi (green panels) and McTigue (orange panels) models. The 1-D histograms are juxtaposed to facilitate comparison of distributions of the four shared parameters. The marked y-axis ranges do not pertain to the nine 1-D histograms, as their y-axes represent frequency counts from MCMC sampling. The dotted lines indicate the MAP value and 95% confidence intervals. Parameters xcen and ycen are relative to Makushin summit (166.925° W, 53.8899° N). Depth (d) is the value below sea level. (For interpretation of the references to colour in this figure legend, the reader is referred to the web version of this article.)

5. Results

The inversion results for the Mogi source and the McTigue source for the 2016–2018 inflation period at Makushin show similar solutions (Fig. 3, Table 2), though the McTigue source MAP value is slightly deeper. Regarding the horizontal location of the intruding magma, the center of the intrusion, according to the Mogi model, was most likely (MAP values) 2.3 km east and 0.3 km north of the summit, falling northwest of the crater. The confidence intervals (for all parameters given at 95%) of the locations are [1.4, 3.2] km for the east direction and [−0.5, 1.1] for the north direction. The McTigue model matches this well with a horizontal position 2.2 km east and 0.2 km north, with confidence intervals of [1.3, 3.2] km east and [−0.6, 1.1] km north. In terms of depth, the Mogi source is most likely about 4.6 km below sea level, with a confidence interval of [2.7, 6.2] km, while the McTigue source is 5.0 km below sea level, with a confidence interval of [3.3,6.8] km. Both models provide a likely increase in cavity volume of 3.8 Mm^3 over the span of two years with confidence intervals of [2.8, 5.4] Mm^3 for the Mogi source and [2.9, 5.6] Mm^3 for McTigue. The estimated McTigue model has a radius of [0.2, 5.7] km, with a MAP value of 1.3 km, but the distribution of this parameter does not appear Gaussian. The Mogi model does not consider the finiteness of the source.

The displacement predictions based on the inversion results align well with observation at all 4 sites whose data are used in the inversion (MAPS, MSWB, AV09, and DUTC) and fall well within the data uncertainties, with residuals less than 1 mm for both models (Fig. 4). The residuals at these sites fall within the bounds of the model uncertainties, which are large at 95% confidence level and thus not shown in the figure. As expected, significant deviations appear at the noisy station MREP that was not included in the inversion for the reasons stated above.

The posterior probability density distribution results for the Yang and Okada models (see supplements S1 for inversion results) show multiple peaks, one-sided distributions, and tradeoffs between parameters, indicating they are not independent of each other or difficult to determine for the respective model geometry. This generally suggests that the model geometries are not a good choice for the data and the estimates of these parameter values are not very reliable. But for the Yang model, the location and depth are still similar to the Mogi/McTigue solutions. More convincingly, out of all models the Mogi model has the smallest residual (residual sum of squares, RSS, Table 2) despite it also having the fewest number of parameters. The residual of the McTigue model is only slightly larger than Mogi, and that of the Yang model is higher but still in the same order of magnitude. Only the Okada model's residual stands out as being notably higher than the other three. Generally, the Mogi source, with the fewest parameters and the least mismatch, would be the most representative of the magma intrusion process. However, given the magma's shallow depth (radius-to-depth ratio is 0.25 for the McTigue solution), we select the McTigue solution as our preferred model and use its parameters for the stress change modeling.

Fig. 5 shows the numerical model results for the Coulomb stress variation, which is obtained by combining the changes in normal stress and shear stress due to the inflating McTigue source. Starting from the volcanic source, in the direction of the inconsistent receiver fault, the variation of normal stress is positive, indicating a reduction of compression, or unclamping of the fault. At the location of the earthquake swarm, the magnitude of the normal stress is approximately 25 kPa (0.25 bar). The shear stress near the source exhibits alternating positive and negative patterns and decreases with distance. At the location of the earthquake swarm, the shear stress shows negative values, ranging from approximately 10 to 20 kPa (0.1–0.2 bar). In the vicinity of the swarm, the Coulomb stress change is positive on the north side and negative on the south side, with magnitudes ranging from approximately −20 to +20 kPa (−0.2 to 0.2 bar). For the events that are consistent with the regional stress field, the Coulomb Stress change is positive, also at 25 kPa (0.25 bar). The relocated swarm information including focal mechanism was provided by Roman et al. (2020).

6. Discussion

For the five GNSS stations located approximately 9–26 km from Makushin, we estimated the position time series of four sites relative to the reference site DUTC (Fig. 2). Site AV09 is only 3 km from the reference site and thus we expected it to move very similarly to DUTC. This is reflected in the stable time series of AV09 relative to DUTC which is scattered around zero during the inflation period (the offset due to the replacement of AV09's antenna could be ignored). All other sites exhibit a clear, temporally coherent 2-year inflation signal between 2016 and 2018 in their time series, despite appreciable variance compared to the signal amplitude. We believe the variance is mostly driven by environmental factors, especially snow and ice on the antenna, which will affect the GPS signal travel path, resulting in biased positions. The velocities estimated from the timeseries are small but spatially coherent, with appreciable, power-law-based uncertainties resulting from the time series variance.

For site MREP, although its northward component shows deformation, the amplitude of periodic seasonal noise throughout the entire time series overwhelms the inflation signal, making it challenging to estimate site velocity at this station accurately, especially in the east-west direction. To ensure the reliability of the inversion and avoid significant biases, we excluded MREP from the analysis, reducing the actual observational data controlling the inversion to twelve data points from four independent stations (null signal in the reference site still constrains the solution).

To reflect our data constraints, one of the five GNSS stations in the Makushin network was selected as reference (DUTC) in the inversion. In addition to the issues with MREP, the standard deviation of the vertical component exceeded the magnitude of the measurements for all sites. Despite these challenges, the inversion succeeded in producing near Gaussian posterior distributions for most parameters that are consistent across several model geometries. The parameters derived from the
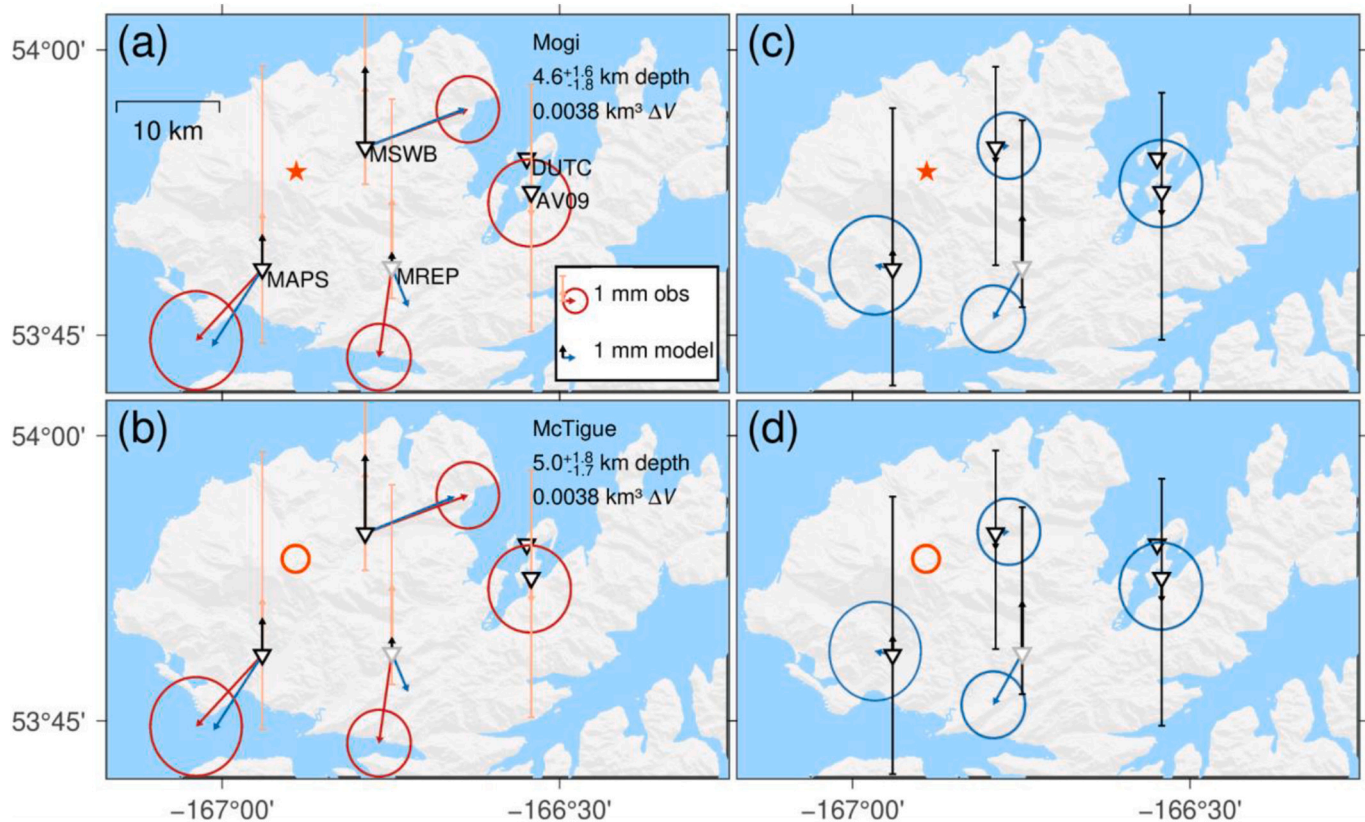
Table 2

Maximum a posteriori (MAP) model parameter values for Mogi, McTigue, Okada, and Yang models. The volume changes of Mogi and McTigue models are directly extracted from the inversion, and those of Okada and Yang models are calculated from inversion results. The depths (d) are the value below sea level.

model	d MAP (km)	d 95% interval [km, km]	ΔV MAP (Mm^3)	ΔV 95% interval	horizontal location MAP (km)	spatial size MAP (km)	geometry angles MAP (°)	RSS (cm^2)
Mogi	4.6	[2.8, 6.2]	3.8	[2.9, 5.4]	x: 2.3 y: 0.3	point	symmetric	0.117
McTigue	5.0	[3.3, 6.8]	3.8	[3.0, 5.5]	x: 2.2 y: 0.2	radius: 1.3	symmetric	0.118
Okada opening dike	5.7	[2.4, 7.3]	7.3	[5.0, 32.7]	x: −0.9 y: 0.5	length: 0.3 width: 0.3	strike: 151 dip: 84	1.52
Yang	4.0	[3.0, 5.6]	2.9	[2.4, 4.1]	x: 2.4 y: −0.1	a: 5.8 b: 1.0	strike: 160 dip: 7	0.245

Fig. 4. Comparison between the observation and model predictions for Mogi (a) and McTigue (b) models, and their residuals (c for Mogi and d for McTigue). Time interval: 2016/01/01 to 2018/01/01. Blue/red arrows indicate horizontal motion, and black/pink arrows are for vertical motion, as listed in the legend panel. Station DUTC is the reference station, its observed/modeled deformation was subtracted from all stations. Data from station MREP (gray) is not used during inversion. Orange star and circle represent the map locations of inferred sources (the circle for the McTigue source also indicates its size). (For interpretation of the references to colour in this figure legend, the reader is referred to the web version of this article.)

tested Mogi, McTigue, and even Yang model were not only remarkably consistent, but they also aligned with previous findings (e.g., Lu and Dzurisin, 2014; Xue and Freymueller, 2020). The probabilistic Bayesian inversion showcased its robustness in handling sparse, low-signal-to-noise-ratio datasets, and demonstrates its benefits over best-fit solutions as the posterior distributions are critical to assessing the model quality.

Our inversion results favor the Mogi and McTigue sources, and based on the shallow depth we favor the McTigue solution despite the slightly degraded fit. Fig. 6 places these source estimates in the context of prior work. Lu et al. (2002) and Lu and Dzurisin (2014) estimated inflation (1993–1995) and deflation (2004–2009) sources, respectively (without confidence intervals). All sources are in similar horizontal locations, yet the new sources are slightly shallower in depth. Our sources, as well as those previously mentioned from earlier studies, fall within the imaged low p-wave velocity regions determined through seismological inversion by Syracuse et al. (2015), which offers compelling evidence for the presence of magma in the region. Thus, the region of active magma dynamics seems to have remained stable over the past 30 years. Our estimate of the magma chamber expansion rate is slightly smaller than that made by Xue and Freymueller (2020) for the same inflation process. This difference is likely due to their choice to only solve for volume change, holding the location similar to the prior, slightly deeper inflation source, requiring a larger volume to produce similar deformation to our slightly shallower source. Moreover, we found that the increase in chamber volume for 2016–2018 inflation (inferred here and by Xue and Freymueller, 2020) is smaller than either historical event investigated.

Based on the hypothesis put forth by Lanza et al. (2022), that a dike-shaped magma intrusion process in 2020 triggered the earthquake swarm, we tested the dike in question. We found that the predicted deformation field caused by the proposed dike is small: even the maximum of the predicted deformation falls well below the sensitivity of GNSS measurements. The proposed dike is practically undetectable with GNSS. Accordingly, no significant deformation signals were observed from the continuous GNSS monitoring throughout 2020. Although MSWB exhibited a westward offset and MAPS showed a northward one, these spatial patterns did not align with those expected from the dike. It is possible that they correspond to the contraction or viscoelastic relaxation of the McTigue source we resolved for 2016–2018. However, due to their minute and ambiguous nature, these signals do not provide sufficient support for a sensible model estimation.

From the GNSS data we identified the described McTigue inflation source. To assess whether the emergence of the earthquake swarm is associated with this inflation source, we utilized ΔCFS analysis. Our FEM simulations predict a Coulomb stress change of approximately 20 kPa (0.2 bar) in the earthquake swarm vicinity, larger than 10 kPa (0.1 bar), the threshold value suggested by Stein (1999) as being influential in inducing earthquakes. Notably, for the events that are inconsistent with the regional stress field, the normal stress change is positive in the swarm region, indicating relief of compression or enhancement of tension, which will reduce the sliding resistance between both sides of the fault. For the consistent ones, the intrusion caused positive Coulomb stress change, intensifying the subduction stress field. Our stress calculation shows that the 2016–2018 intrusion at the current magma source encourages earthquakes in the swarm region, which is supported by the slight unclamping in the earthquake region (Fig. 5).

Furthermore, we analyzed the principal stresses from the stress change field generated by magma intrusion at the site of the M4.2
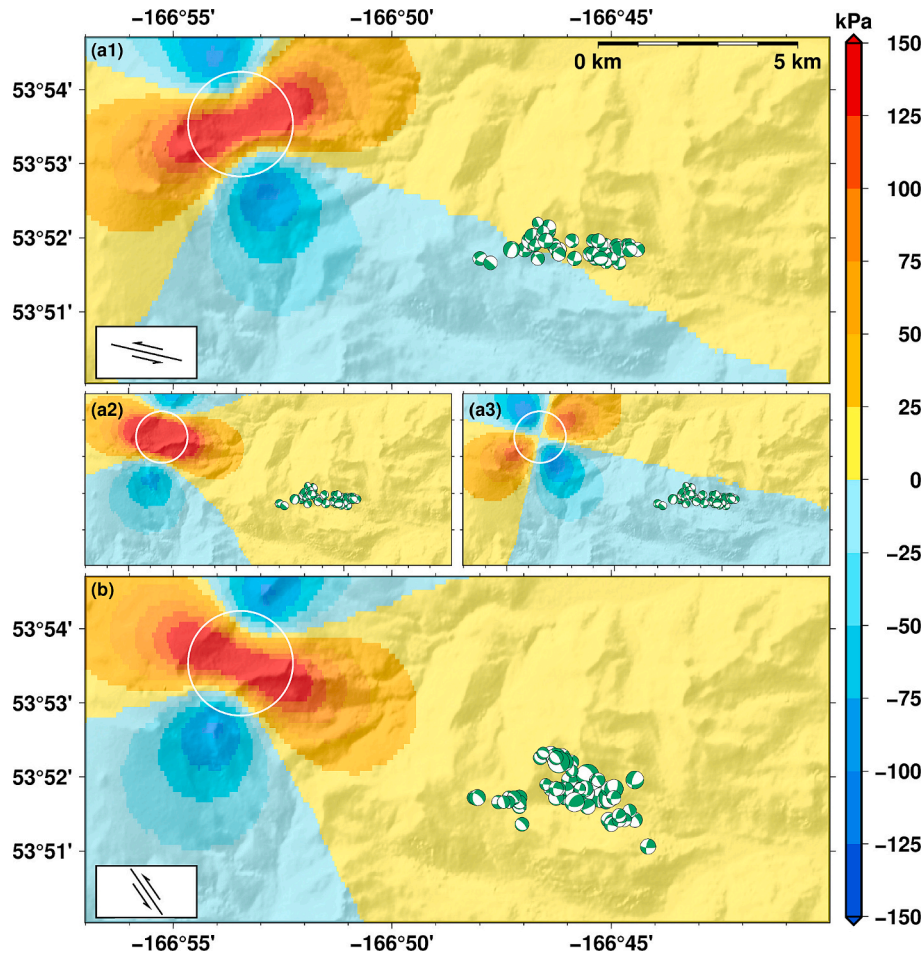
Fig. 5. Numerical modeling result for stress changes due to the inferred McTigue source: (a1) Coulomb stress change for inconsistent events; normal stress (a2) and shear stress (a3) change for inconsistent events; (b) Coulomb stress change for consistent events. Receiver faults for the calculation are left-lateral pure strike-slip faults with 105° strike for inconsistent events and 327° for consistent ones (see insets). Each green circle with a focal mechanism represents a relocated earthquake in the 2020 Makushin swarm. All panels are calculated at 7 km depth, where most of the earthquakes locate. The white circle represents the McTigue source with a 1.3 km MAP radius. (For interpretation of the references to colour in this figure legend, the reader is referred to the web version of this article.)
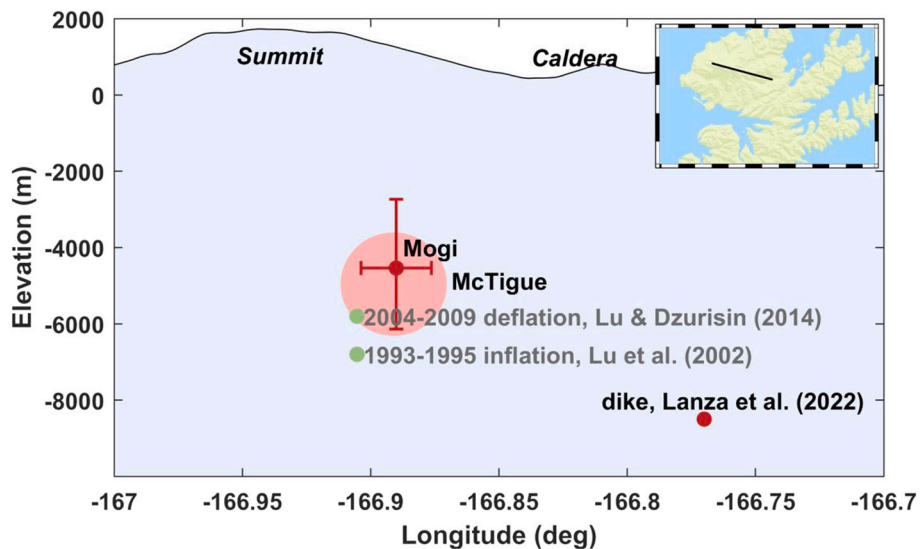

Fig. 6. Comparison of models on a vertical cross-section, marked as the black line in the inset panel. The markers indicate the projected location of several sources on this cross-section. In the direction perpendicular to the plane, the fluctuations of the source positions are small.

earthquake. Our calculation shows that the predicted strike of the first principal stress was 290°, closely aligning with the observed strike of the maximum compression (P-axis, 303°). This indicates that the intrusion exacerbated the forces acting on the M4.2 earthquake, contributing to its occurrence. Similarly, the direction of the first principal stress for the M4.1 earthquake also suggests the role of intrusion in promoting the occurrence of this event.

Plate subduction and magmatic intrusion are not the sole sources of stress change in the swarm area. Earthquakes earlier in the swarm, and their resulting stress changes impact subsequent events. According to Lanza et al. (2022), the Coulomb stress changes produced by the two largest earthquakes in the swarm are 20 times greater than those caused by the magmatic intrusion. Moreover, most earthquakes in the swarm are located within the positive Coulomb stress change area triggered by these two earthquakes. While the early M4 earthquakes appear to be encouraged by the intrusion, the locally much larger stress changes from these events likely dominated the occurrence of the swarm, which we consider a result of the combined effects of plate subduction, magmatic intrusion, and the early major earthquakes.

The 2.5-year interval between the inflation and the swarm may indicate a delayed static triggering process (e.g., Savage and Cockerham, 1984; Thatcher and Savage, 1982), or a creep-behaved dynamic triggering described in Shelly et al. (2011). It is hard to determine whether delayed seismicity is common at Makushin, because the magma movement was continuous during previous monitored periods: there was a swarm in 1997, within the 1996–2001 deflation period; a swarm in 2002, within the 2001–2004 inflation; then a swarm in 2004, within the 2004–2009 deflation (Dixon et al., 2020).

7. Conclusions

We analyzed the 2016–2020 unrest period of Makushin volcano. Geodetically, the 2016–2018 portion taken from the continuous GNSS observations at Makushin volcano revealed the presence of surface inflation during this period. The 1-cm surface inflation pattern during this period is modeled as magma intrusion. The maximum a posteriori source is located east of the summit, under the caldera, and 5 km deep below sea level. The volume of the reservoir increased by 0.004 km^3. Our modeling is in agreement with previous sources for other deformation episodes and reveals a new phase in the time series of Makushin magma system movements over the past three decades.

The magma intrusion process can cause a 20-kPa increase in ΔCFS at the earthquake swarm region. Stress analysis suggests the magma intrusion encouraged the initial M4 earthquakes and contributed to the earthquake swarm. A more detailed analysis (perhaps considering viscoelasticity) with the respective physically reasonable assumptions may provide further insights.

Our study highlights the importance of long-term GNSS observations in tracking volcanic deformation and provides an example for volcano-earthquake interaction. As one of the most active volcanoes on the Aleutian Arc, Makushin seems to have maintained a relatively stable active part of its magmatic system since its last eruption in 1995.

CRediT authorship contribution statement

Yitian Cheng: Data curation, Methodology, Validation, Writing – original draft, Writing – review & editing. **Ronni Grapenthin:** Conceptualization, Funding acquisition, Investigation, Resources, Supervision, Writing – original draft, Writing – review & editing.

Declaration of competing interest

The authors declare that they have no known competing financial interests or personal relationships that could have appeared to influence the work reported in this paper.

Appendix A. Supplementary data

Supplementary data to this article can be found online at https://doi.org/10.1016/j.jvolgeores.2024.108010.

References

Agnew, D.C., 2012. SPOTL: Some Programs for Ocean-Tide Loading.

Altamimi, Z., Rebischung, P., Métivier, L., Collilieux, X., 2016. ITRF2014: a new release of the International Terrestrial Reference Frame modeling nonlinear station motions. J. Geophys. Res. Solid Earth 121 (8), 6109–6131.

Angarita, M., R. Grapenthin, S. Henderson, M. Christoffersen, K. Anderson, Versatile Modeling Of Deformation (VMOD) Inversion Framework: Application to 20 years of observations at Westdahl Volcano and Fisher Caldera, Alaska, US, submitted to G3.

Aster, R.C., Borchers, B., Thurber, C.H., 2018. Parameter Estimation and Inverse Problems. Elsevier.

Baer, G., Hamiel, Y., Shamir, G., Nof, R., 2008. Evolution of a magma-driven earthquake swarm and triggering of the nearby Oldoinyo Lengai eruption, as resolved by InSAR, ground observations and elastic modeling, East African Rift, 2007. Earth Planet. Sci. Lett. 272 (1–2), 339–352.

Bertiger, W., Bar-Sever, Y., Dorsey, A., Haines, B., Harvey, N., Hemberger, D., Heflin, M., Lu, W., Miller, M., Moore, A.W., Murphy, D., 2020. GipsyX/RTGx, a new tool set for space geodetic operations and research. Adv. Space Res. 66 (3), 469–489.

Biggs, J., Ebmeier, S.K., Aspinall, W.P., Lu, Z., Pritchard, M.E., Sparks, R.S.J., Mather, T.A., 2014. Global link between deformation and volcanic eruption quantified by satellite imagery. Nat. Commun. 5 (1), 3471.

Blewitt, G., Hammond, W.C., Kreemer, C., 2018. Harnessing the GPS data explosion for interdisciplinary science. Eos 99. https://doi.org/10.1029/2018EO104623.

Böhm, J., Möller, G., Schindelegger, M., Pain, G., Weber, R., 2015. Development of an improved empirical model for slant delays in the troposphere (GPT2w). GPS Solutions 19 (3), 433–441.

Cayol, V., Dieterich, J.H., Okamura, A.T., Miklius, A., 2000. High magma storage rates before the 1983 eruption of Kilauea, Hawaii. Science 288 (5475), 2343–2346.

Chaussard, E., Amelung, F., 2012. Precursory inflation of shallow magma reservoirs at west Sunda volcanoes detected by InSAR. Geophys. Res. Lett. 39 (21).

DeMets, C., Gordon, R.G., Argus, D.F., Stein, S., 1994. Effect of recent revisions to the geomagnetic reversal time scale on estimates of current plate motions. Geophys. Res. Lett. 21 (20), 2191–2194.

Dixon, J.P., Cameron, C.E., Iezzi, A.M., Power, J.A., Wallace, K., and Waythomas, C.F., (2020), 2017 Volcanic Activity in Alaska-Summary of Events and Response of the Alaska Volcano Observatory: *U.S.* Geological Survey Scientific Investigations Report 2020–5102 61., doi: https://doi.org/10.3133/sir20205102.

Dow, J.M., Neilan, R.E., Rizos, C., 2009. The international GNSS service in a changing landscape of global navigation satellite systems. J. Geod. 83 (3), 191–198.

Ebmeier, S.K., Andrews, B.J., Araya, M.C., Arnold, D.W.D., Biggs, J., Cooper, C., Cottrell, E., Furtney, M., Hickey, J., Jay, J.J.J.A.V., Lloyd, R., 2018. Synthesis of global satellite observations of magmatic and volcanic deformation: implications for volcano monitoring & the lateral extent of magmatic domains. J. Appl. Volcanol. 7 (1), 1–26.

Egbert, G.D., Erofeeva, S.Y., 2002. Efficient inverse modeling of barotropic ocean tides. J. Atmos. Ocean. Technol. 19 (2), 183–204.

Elliott, J., Freymueller, J.T., 2020. A block model of present-day kinematics of Alaska and western Canada. J. Geophys. Res. Solid Earth 125 (7) p.e2019JB018378.

Elsworth, D., Voight, B., 1995. Dike intrusion as a trigger for large earthquakes and the failure of volcano flanks. J. Geophys. Res. Solid Earth 100 (B4), 6005–6024.

Fernández, J., Pepe, A., Poland, M.P., Sigmundsson, F., 2017. Volcano Geodesy: recent developments and future challenges. J. Volcanol. Geotherm. Res. 344, 1–12.

Freymueller, Jeffrey T., Grapenthin, Ronni, 2013. Alaska Volcano Observatory GPS Network - DUTC-Dutch Harbor AVO P.S., UNAVCO, GPS/GNSS Observations Dataset. https://doi.org/10.7283/T51G0JPJ.

Freymueller, Jeffrey T., Grapenthin, Ronni, Paskievitch, John, 2011. Alaska Volcano Observatory GPS Network Makushin - MSWB-MSWB P.S., UNAVCO, GPS/GNSS Observations Dataset. https://doi.org/10.7283/T5668BJ3.

Freymueller, Jeffrey T., Grapenthin, Ronni, Paskievitch, John, 2012a. Alaska Volcano Observatory GPS Network - MAPS-Makushin Pakushin SE P.S., UNAVCO, GPS/GNSS Observations Dataset. https://doi.org/10.7283/T5T151S7.

Freymueller, Jeffrey T., Grapenthin, Ronni, Paskievitch, John, 2012b. Alaska Volcano Observatory GPS Network - MREP-Makushin Repeater P.S., UNAVCO, GPS/GNSS Observations Dataset. https://doi.org/10.7283/T5P8492X.

Grapenthin, R., Kyle, P., Aster, R.C., Angarita, M., Wilson, T., Chaput, J., 2022a. Deformation at the open-vent Erebus volcano, Antarctica, from more than 20 years of GNSS observations. J. Volcanol. Geotherm. Res. 432, 107703.

Grapenthin, R., Cheng, Y., Angarita, M., Tan, D., Meyer, F.J., Fee, D., Wech, A., 2022b. Return from Dormancy: Rapid inflation and Seismic Unrest Driven by Transcrustal Magma transfer at Mt. Edgecumbe (L'úx Shaa) Volcano, Alaska. Geophys. Res. Lett. 49 (20) p.e2022GL099464.

Haario, H., Saksman, E., Tamminen, J., 2001. An adaptive Metropolis algorithm. Bernoulli 223–242.

Hastings, W.K., 1970. Monte Carlo sampling methods using Markov chains and their applications. Biometrika 57 (1), 97–109. https://doi.org/10.1093/biomet/57.1.97.

Heap, M.J., Villeneuve, M., Albino, F., Farquharson, J.I., Brothelande, E., Amelung, F., Got, J.L., Baud, P., 2020. Towards more realistic values of elastic moduli for volcano modelling. J. Volcanol. Geotherm. Res. 390, 106684.

Herring, T.A., Melbourne, T.I., Murray, M.H., Floyd, M.A., Szeliga, W.M., King, R.W., Phillips, D.A., Puskas, C.M., Santillan, M., Wang, L., 2016. Plate Boundary Observatory and related networks: GPS data analysis methods and geodetic products. Rev. Geophys. 54 (4), 759–808.

Hooper, A., Ófeigsson, B., Sigmundsson, F., et al., 2011. Increased capture of magma in the crust promoted by ice-cap retreat in Iceland. Nat. Geosci. 4, 783–786.

King, G.C., Stein, R.S., Lin, J., 1994. Static stress changes and the triggering of earthquakes. Bull. Seismol. Soc. Am. 84 (3), 935–953.

Lanza, F., Roman, D.C., Power, J.A., Thurber, C.H., Hudson, T., 2022. Complex magmatic-tectonic interactions during the 2020 Makushin Volcano, Alaska, earthquake swarm. Earth Planet. Sci. Lett. 587, 117538.

Larsen, J.F., Schaefer, J., Vallance, J.W., Neill, O.K., 2020. Petrology and geochemistry of three early Holocene eruptions from Makushin Volcano, Alaska. Bull. Volcanol. 82, 1–17.

Lazecký, M., Spaans, K., González, P.J., Maghsoudi, Y., Morishita, Y., Albino, F., Elliott, J., Greenall, N., Hatton, E., Hooper, A., Juncu, D., 2020. LiCSAR: an automatic InSAR tool for measuring and monitoring tectonic and volcanic activity. Remote Sens. 12 (15), 2430.

Lerner, A.H., Crowley, P.D., Nicolaysen, K.P., Hazlett, R.W., 2018. Stratigraphy, distribution, and evidence for mafic triggering of the ca. 8.5 ka Driftwood Pumice eruption, Makushin Volcano, Alaska, USA. J. Volcanol. Geotherm. Res. 357, 362–377.

Lu, Z., Dzurisin, D., 2014. InSAR imaging of Aleutian volcanoes. In: InSAR Imaging of Aleutian Volcanoes. Springer, Berlin, Heidelberg, pp. 87–345.

Lu, Z., Power, J.A., McConnell, V.S., Wicks Jr., C., Dzurisin, D., 2002. Preeruptive inflation and surface interferometric coherence characteristics revealed by satellite radar interferometry at Makushin Volcano, Alaska: 1993–2000. J. Geophys. Res. Solid Earth 107 (B11).

McGimsey, R.G., Neal, C.A., 1996. 1995 Volcanic activity in Alaska and Kamchatka; Summary of events and Response of the Alaska Volcano Observatory: U. S. Geological Survey Open-File Report 96-738, p. 22. https://pubs.usgs.gov/of/1 996/0738/.

McTigue, D.F., 1987. Elastic stress and deformation near a finite spherical magma body: Resolution of the point source paradox. J. Geophys. Res. 92 (B12), 12931–12940. https://doi.org/10.1029/JB092iB12p12931.

Miller, T.P., McGimsey, R.G., Richter, D.H., Riehle, J.R., Nye, C.J., Yount, M.E., Dumoulin, J.A., 1998. Catalog of the Historically Active Volcanoes of Alaska. United States Department of the Interior, United States Geological Survey, p. 104.

Mogi, K., 1958. Relations between the eruptions of various volcanoes and the deformation of the ground surfaces around them. Bulletin of the Earthquake Research Institute, University of Tokyo 36, 99–134.

Okada, Y., 1992. Internal deformation due to shear and tensile faults in a half-space. Bull. Seismol. Soc. Am. 82 (2), 1018–1040.

Patil, A., Huard, D., Fonnesbeck, C.J., 2010. PyMC: Bayesian stochastic modelling in Python. J. Stat. Softw. 35 (4), 1.

Pedersen, R., Sigmundsson, F., Einarsson, P., 2007. Controlling factors on earthquake swarms associated with magmatic intrusions; Constraints from Iceland. J. Volcanol. Geotherm. Res. 162 (1–2), 73–80.

Phillipson, G., Sobradelo, R., Gottsmann, J., 2013. Global volcanic unrest in the 21st century: an analysis of the first decade. J. Volcanol. Geotherm. Res. 264, 183–196. https://doi.org/10.1016/j.jvolgeores.2013.08.004.

Poland, M.P., de Zeeuw-van Dalfsen, E., 2021. Volcano geodesy: A critical tool for assessing the state of volcanoes and their potential for hazardous eruptive activity. In: Forecasting and Planning for Volcanic Hazards, Risks, and Disasters. Elsevier, pp. 75–115.

Pritchard, M.E., Mather, T.A., McNutt, S.R., Delgado, F.J., Reath, K., 2019. Thoughts on the criteria to determine the origin of volcanic unrest as magmatic or non-magmatic. Phil. Trans. R. Soc. A 377 (2139), 20180008.

Roman, D.C., Lanza, F., Power, J.A., Thurber, C.H., 2020, December. Insights into the 2020 Earthquake Swarm at Makushin Volcano, alaska from relative relocations and focal mechanisms. In: AGU Fall Meeting Abstracts, 2020. V020-0006.

Savage, J.C., Cockerham, R.S., 1984. Earthquake swarm in Long Valley caldera, California, January 1983: evidence for dike inflation. J. Geophys. Res. Solid Earth 89 (B10), 8315–8324.

Segall, P., 2010. Earthquake and volcano deformation. In: Earthquake and Volcano Deformation. Princeton University Press.

Shelly, D.R., Peng, Z., Hill, D.P., Aiken, C., 2011. Triggered creep as a possible mechanism for delayed dynamic triggering of tremor and earthquakes. Nat. Geosci. 4 (6), 384–388.

Sigmundsson, F., Parks, M., Pedersen, R., Jónsdóttir, K., Ófeigsson, B.G., Grapenthin, R., Dumont, S., Einarsson, P., Drouin, V., Heimisson, E.R., Hjartardóttir, Á.R., 2018. Magma movements in volcanic plumbing systems and their associated ground deformation and seismic patterns. In: Volcanic and Igneous Plumbing Systems. Elsevier, pp. 285–322.

Stein, R., 1999. The role of stress transfer in earthquake occurrence. Nature 402, 605–609. https://doi.org/10.1038/45144.

Syracuse, E.M., Maceira, M., Zhang, H., Thurber, C.H., 2015. Seismicity and structure of Akutan and Makushin Volcanoes, Alaska, using joint body and surface wave tomography. J. Geophys. Res. Solid Earth 120 (2), 1036–1052.

Thatcher, W., Savage, J.C., 1982. Triggering of large earthquakes by magma-chamber inflation, Izu Peninsula, Japan. Geology 10 (12), 637–640.

UNAVCO Community, 2004. PBO GPS Network - AV09-Haystack_AK2004 P.S., UNAVCO, GPS/GNSS Observations Dataset. https://doi.org/10.7283/T5GQ6VP0.

Walter, T.R., Amelung, F., 2006. Volcano-earthquake interaction at Mauna Loa volcano, Hawaii. J. Geophys. Res. Solid Earth 111 (B5).

Williams, S.D.P., 2008. CATS: GPS coordinate time series analysis software. GPS Solutions 12, 147–153. https://doi.org/10.1007/s10291-007-0086-4.

Xue, X., Freymueller, J.T., 2020. A 25-year history of Volcano Magma Supply in the East Central Aleutian Arc, Alaska. Geophys. Res. Lett. 47 e2020GL088388.

Yang, X.-M., Davis, P.M., Dieterich, J.H., 1988. Deformation from inflation of a dipping finite prolate spheroid in an elastic half-space as a model for volcanic stressing. J. Geophys. Res. 93 (B5), 4249–4257. https://doi.org/10.1029/JB093iB05p04249.